ACS APPLIED MATERIALS & INTERFACES

www.acsami.org

Research Article

Role of Interfacial Morphology in Cu_2O/TiO_2 and Band Bending: Insights from Density Functional Theory

Mona Asadinamin, Aleksandar Živković,* Nora H. de Leeuw, and Steven P. Lewis*

Cite This: ACS Appl. Mater. Interfaces 2024, 16, 35781−35792

Read Online

ACCESS | Metrics & More | Article Recommendations | Supporting Information

ABSTRACT: Photocatalysis, a promising solution to environmental challenges, relies on the generation and utilization of photogenerated charge carriers within photocatalysts. However, the recombination of these carriers often limits efficiency. Heterostructures, especially Cu_2O/TiO_2, have emerged as effective solutions to enhance charge separation. This study systematically explores the effect of interfacial morphologies on the band bending within Cu_2O/TiO_2 anatase heterostructures by employing density functional theory. Through this study, eight distinct interfaces are identified and analyzed, revealing a consistent staggered-type band alignment. Despite variations in band edge positions, systematic charge transfer from Cu_2O to TiO_2 is observed across all interfaces. The proposed band bending configurations would suggest enhanced charge separation and photocatalytic activity under ultraviolet illumination due to a *Z*-scheme configuration. This theoretical investigation provides valuable insights into the interplay between interfacial morphology, band bending, and charge transfer for advancing the understanding of fundamental electronic mechanisms in heterostructures.

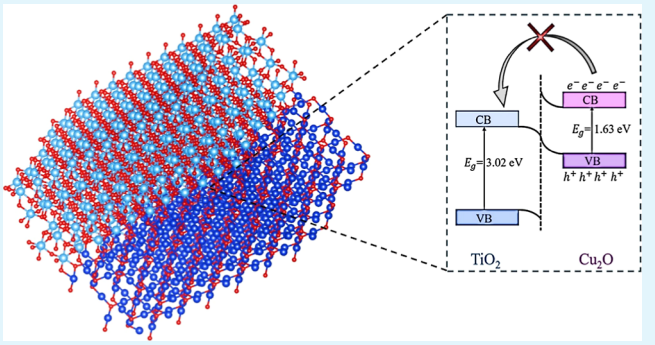

KEYWORDS: *heterostructures, Cu_2O/TiO_2, anatase, density functional theory, DFT, interface, band bending, Z-scheme, photocatalysis*

INTRODUCTION

Photocatalysis, a promising solution to environmental challenges such as air purification and wastewater treatment, operates via the absorption of photons to create charge carriers (electron−hole pairs) within a photocatalyst. These photogenerated charge carriers are then anticipated to participate in surface redox reactions that fuel the photocatalytic process. A challenge, however, is the tendency of the photogenerated electrons and holes to recombine, which deactivates the charge carriers before they can contribute to the desired photocatalytic reactions. Particularly in single photocatalysts, the lack of a suitable mechanism to efficiently separate and transport these charge carriers often leads to high recombination rates. Various strategies have been proposed to overcome these limitations, such as surface modification,[1,2] metal or nonmetal doping,[3,4] etc. Among these, heterostructures have emerged as effective solutions by significantly enhancing efficiency via charge separation.[5,6] Key benefits include improved separation of photogenerated charge carriers, achieved through staggered band alignments across different materials, leading to reduced recombination rates and longer charge carrier lifetimes. Furthermore, materials like TiO_2, while exhibiting excellent photocatalytic performance, suffer from a wide band gap, limiting their effectiveness under visible light. By the formation of heterostructures, it is possible to combine such compounds with narrow band gap materials to enhance the utilization of the visible light spectrum.

In a heterostructure, when two semiconductor materials meet at the junction, their differing energy band gaps and band edge positions cause an initial discontinuity in the Fermi energy. To reach equilibrium, electrons and holes migrate in opposing directions. This charge transport gives rise to an interfacial space charge region, stemming from the electric field, which consequently results in band bending.[7] Depending on the relative band edges and configuration of band bending, semiconductor interfaces can be organized into four types of heterojunctions: straddling gap (type I), staggered gap (type II), *Z*-scheme, or broken gap (type III).[8] Type II and *Z*-scheme interfaces can reduce electron−hole recombination and increase the migration of specific charge carriers to the semiconductor surface, enhancing the photocatalytic reactions. Identifying the band bending configuration is key to predicting the fundamental photocatalytic mechanisms of heterostructures.

Received: April 14, 2024
Revised: June 7, 2024
Accepted: June 10, 2024
Published: June 26, 2024

In evaluating the band bending at interfaces, the morphology of materials can influence their interfacial band structure and band bending properties.[9,10] With advancements in novel growth techniques, such as molecular-beam epitaxy, epitaxial interfaces of exceptional quality can be fabricated.[11] This is achievable not just between lattice-matched semiconductors but also between materials with considerable differences in their lattice constants.[12] When these lattice mismatches are present, uniform lattice strain can accommodate them if the layers are sufficiently thin.[13] These strains introduce alterations to electronic properties, offering enhanced versatility in designing semiconductor devices.[13] The interplay between structural and electronic properties at interfaces can be explored both experimentally and theoretically, with each technique coming with its own set of opportunities and obstacles. Density functional theory (DFT) calculations as well as experimental methods, like in situ X-ray photoelectron spectroscopy and scanning transmission electron microscopy (TEM), reveal that structural changes, including planar defects,[14] elastic strain,[15] tensile strain,[16] and introduction of impurities and vacancies[17] affect the electronic transport properties of the interface. Specifically, these changes influence band edge offsets, enabling tunable band bending properties for photocatalytic applications. However, from a computational point of view, a challenge persists in determining the precise atomic structure at interfaces, given that acquiring experimental data on interfacial morphologies often proves elusive.[18] Direct observation of interfacial atomic structures using high-resolution TEM is challenging, primarily because of the limited reflections from lattice planes, which make it difficult to ascertain actual atom positions,[19] and high-resolution observations of these interfacial geometries remain a formidable task.[20] As a result, the detailed atomic structure and compositional data of interfaces required for precise first-principles calculations of their electronic properties are often lacking. This underscores the importance of a comprehensive theoretical investigation and systematical exploration of various interfacial morphologies, accounting for different degrees of lattice mismatch, and analyzing their impact on the electronic and band bending properties of heterostructures.

Theoretical calculations have been employed for a long time to study the electronic properties of interfaces. While earlier methods leaned on more basic techniques such as effective dipole models,[21] tight-binding schemes,[22] or empirical rules,[23] in the recent few decades, DFT has been utilized as an advanced computational to study band offset and interfacial dipole in heterostructures.[24,25] Despite the valuable contributions of DFT studies in this area, several limitations persist. The majority of investigations lack precise predictions due to the absence of explicit heterostructure calculations.[26−29] Additionally, many studies tend to focus on arbitrary surface orientations of the individual components rather than considering the most dominant orientations from experimental observations, and more importantly, arbitrarily chosen interfacial morphologies, which may not accurately sketch the full picture of all the possible configurations and their effect on band bending.[30−32]

In this study, two well-known photocatalysts, TiO_2 and Cu_2O, have been selected to study the morphological effect on their interfacial electronic properties. TiO_2—a prominent photocatalyst due to its remarkable photocatalytic properties[33,34]—has been frequently paired with Cu_2O—an abundant, low-cost, and well-studied effective photocatalyst[35]—demonstrating enhanced charge transfer rates and reduced electron−hole recombination.[33,36] This heterostructure mitigates the main drawback of TiO_2, which is its large band gap (∼3.2 eV[37]), by pairing it with Cu_2O, a lower band gap material (∼2.2 eV[38]). The incorporation of Cu_2O facilitates the extension of light absorption into the visible spectrum, thereby optimizing the use of solar energy.[33] Furthermore, both materials have appropriate band edges with respect to the redox potential of many pollutants,[39,40] facilitating the requisite redox reactions by ensuring that the photogenerated electrons in the conduction band (CB) have adequate energy for reduction reactions, while the holes in the valence band (VB) possess sufficient energy for oxidation reactions. Numerous experimental studies have been conducted to examine the interfacial band edges of Cu_2O/TiO_2. While the majority of investigations have reported a staggered (type II or *Z*-scheme) heterojunction featuring Cu_2O band edges situated above the TiO_2 band edges,[29,41−43] a limited number of studies have identified a straddling (type I) heterojunction with the VB and CB of Cu_2O positioned within the band gap of TiO_2.[33,44] This has led to a debate regarding the nature of the heterostructure between type II, *Z*-scheme, and I configurations. Despite a great number of experimental studies, theoretical studies on Cu_2O/TiO_2 remain scarce.[45,46] Although experimental research has provided valuable insights into the interfacial properties of Cu_2O/TiO_2, a more comprehensive understanding of the electronic properties at the interface is still needed, particularly from a theoretical standpoint. In this study, we mapped all the possible interfacial morphologies of Cu_2O/TiO_2 and, by assessing the chemistry of interfacial bonding, quantifying the strain magnitude, and considering the size of the system in relation to the computational feasibility, we identified eight distinct interfacial morphologies to study their band bending properties. Despite the variation in the morphology of the interfaces and the level of strain, we observed similar electronic properties and band bending behavior across all the heterostructures.

COMPUTATIONAL DETAILS

All calculations were carried out based on the framework of generalized Kohn−Sham scheme[47] as implemented in the Vienna ab initio simulation package (VASP),[48,49] employing PBE[50,51] and Heyd−Scuseria−Ernzerhof (HSE06) hybrid functional.[52−54] The electron−core interactions have been described by means of the projected augmented wave (PAW) method.[49,55] Soft PAW potentials were used for Cu, O, and Ti atoms. The electronic wave functions were expanded in plane waves with an energy cutoff of 550 eV. The Brillouin zone was sampled using the Monkhorst−Pack special *k*-point mesh.[56] The convergence threshold for total energy self-consistency was kept at 10^{-6} eV. The atomic coordinates and unit cell parameters have been optimized using the conjugate gradient method until the force on each atom was less than 0.01 eV $Å^{-1}$. TiO_2 in its anatase phase has been used because of its superior photocatalytic activity.

The crystal configuration of Cu_2O is defined by a cubic lattice structure, characterized by the $Pn\bar{3}m$ space group. Its unit cell contains four copper (Cu) and two oxygen (O) atoms. The crystal configuration of TiO_2 (titanium dioxide) in its anatase form is defined by a tetragonal lattice structure, which is characterized by the $I4_1/amd$ space group. Its unit cell contains four titanium (Ti) and eight O atoms. The computed lattice parameters using PBE functional for Cu_2O are a_{Cu_2O} =

https://doi.org/10.1021/acsami.4c06081
ACS Appl. Mater. Interfaces 2024, 16, 35781−35792

4.267 Å, and for TiO_2 are a_{TiO_2} = 3.807 Å and c_{TiO_2} = 9.707 Å, in good agreement with the experimental findings of $a^{exp}_{Cu_2O} \sim 4.269$ Å,[57] $a^{exp}_{TiO_2} \sim 3.78$ Å,[58,59] and $c^{exp}_{TiO_2} \sim 9.50$ Å.[58,59]

In order to design a realistic model system of the Cu_2O/TiO_2 heterojunction, we have considered the $Cu_2O(111)$ and the TiO_2-anatase (101) nonpolar surfaces, being the most stable and dominant terminations across diverse morphologies and fabrication techniques.[28,33,60] The surfaces were modeled as two-dimensional periodic slabs, with a vacuum layer separating the periodic images in the z-direction. A vacuum region at 20 Å was tested to be sufficient to avoid the superficial interactions between the periodic slabs. The in-plane lattice constants are fixed to the optimized bulk values, and only the internal coordinates are relaxed. To characterize the surfaces, the surface energy (γ) as a measure of the thermodynamic stability has been calculated through the following expression

$$\gamma = \frac{E(n) - nE_{bulk}}{2A} \quad (1)$$

where $E(n)$ is the energy of the slab containing n layers, E_{bulk} the energy of the bulk, and A the area of one side of the slab.

The specific adhesive energy, a measure of the energy gained once the interface boundary between two surfaces (s1 and s2) is formed, is given by

$$\beta_{s1/s2} = \frac{E_{s1} + E_{s2} - E_{s1/s2}}{A} \quad (2)$$

where E_{s1} and E_{s2} are total energies of the respective slabs and $E_{s1/s2}$ is the final interface energy.

The specific interface energy, defined as the excess energy resulting from the energy balance described by the Dupré's relation,[61] is given by

$$\gamma_{s1/s2} = \gamma_{s1} + \gamma_{s2} - \beta_{s1/s2} \quad (3)$$

where γ_{s1} and γ_{s2} are surface energies of the respective slabs forming the interface, and $\beta_{s1/s2}$ the adhesion energy defined earlier.

The planar and macroscopic averaged potentials as well as the charge density differences were computed using the VASPKIT post-processing code.[62] Graphical drawings were produced using VESTA[63] and OVITO.[64]

The vertical ionization potential (IP) is calculated using a bulk-based definition, via the electrostatic alignment between the surface and the bulk as follows[65]

$$\varepsilon_{IP} = \Delta\varepsilon_{vac\text{-}ref} - \Delta\varepsilon_{VBM\text{-}ref}$$

where $\Delta\varepsilon_{vac\text{-}ref}$ is the difference between the electrostatic potential in the vacuum region and the bulk-like reference level in the slab (the 1s states of Cu and Ti in the middle of the $Cu_2O(111)$ and $TiO_2(101)$ slabs, respectively). The second term, $\Delta\varepsilon_{VBM\text{-}ref}$, is the difference in the eigenvalue energy between the VB maximum (VBM) and reference level from bulk calculations. The electron affinity (EA) is obtained by subtracting the obtained bang gap value from the IP.

The macroscopic average of the electrostatic potential along the nonperiodic direction of the interfaces was computed using the MacroDensity package.[66]

The heterostructures with different degrees of lattice mismatch (strain) were generated using the QuantumATK software developed by Synopsys,[67] which provides a user-friendly setting to adjust the lattice vectors and align the crystal structures to create the desired heterostructures. In generating the interfaces, Cu_2O was subjected to strain (treated as a film), a consequence of its deposition as the top layer in the Cu_2O/TiO_2 fabrication process.[68,69]

RESULTS AND DISCUSSION

Surfaces. Determining suitable surface orientations for the construction of a heterostructure poses a challenge due to its impact on band bending characteristics. This challenge arises from the involvement of surface dipoles in the determination of the VB and CB edges, which are critical factors in establishing interfacial band alignment. These band positions are intrinsically influenced by the surface orientation, composition, atomistic structure, and electronic structure, all of which collectively contribute to the surface dipole effects.[70,71] From a computational standpoint, a key constraint in selecting the right surfaces is the assessment of surface polarity, as polar surfaces inherently exhibit a notable electrostatic instability.[72] This instability arises from the presence of macroscopic dipoles oriented perpendicular to the surface within each unit cell that accumulate, necessitating the introduction of compensating charges to neutralize these dipoles. Achieving such compensation in practice involves extensive surface modifications, including significant adjustments in stoichiometry, faceting, spontaneous desorption of atoms, large-cell reconstruction due to the ordering of surface vacancies, among other complex processes.[73]

Experimentally, the primary surfaces in heterostructures are identified through high-resolution TEM analysis. This method unveils predominant lattice spacings, facilitating determination of the corresponding surfaces for each constituent material within the heterostructure. In the specific case of the Cu_2O/TiO_2 heterojunction, surfaces (111) and (101) have consistently emerged as the dominant surfaces for Cu_2O and TiO_2, respectively, across diverse morphologies and fabrication techniques.[33,60] Notably, these surfaces exhibit nonpolar characteristics, showing no electrostatic instabilities. Therefore, in the current study, surfaces (111) and (101) are selected for Cu_2O and TiO_2, respectively.

The initial geometry of the slabs for a 4-bilayer TiO_2 and a 6-trilayer Cu_2O is shown in Figure S1. The thickness of the surfaces was optimized with respect to the surface energy (eq 1). The results using the PBE functional are presented in Figure S2, which indicate that the surface energy quickly converged to a value of 1.13 J/m^2 for a 4-bilayer TiO_2 and 0.77 J/m^2 for a 6-trilayer Cu_2O, in agreement with the earlier studies.

Interfaces. *Geometry.* To construct the interfaces, we have confined this study to epitaxial heterostructures, with lattice mismatch values predominantly confined within a 10% threshold.[74] It is well-established that an escalated degree of lattice mismatch can lead to the formation of defects in the heterostructure, such as dislocations, threading dislocations, misfit dislocations, and cracks.[75] Severe lattice mismatch will cause dislocations at the interface and results in electrical defects such as interface traps.[76] These defects can significantly degrade the electronic and optical properties of the heterostructure, which can limit their practical applications. Figure 1 shows a map of all the possible heterostructure of $Cu_2O(111)/TiO_2(101)$ as a function of the mean absolute strain (lattice mismatch)—which is defined as $\frac{a_{TiO_2} - a_{Cu_2O}}{a_{TiO_2}}$,

https://doi.org/10.1021/acsami.4c06081
ACS Appl. Mater. Interfaces 2024, 16, 35781−35792

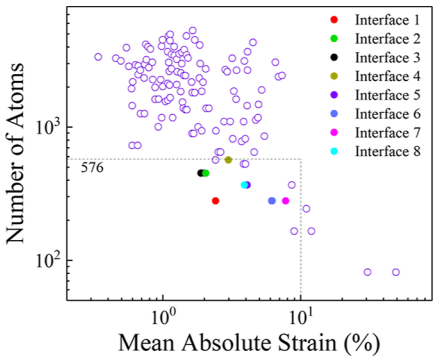

Figure 1. Map of all the possible heterostructures of $Cu_2O(111)/TiO_2(101)$ as a function of lattice mismatch (as defined in the text) and total number of atoms in the unit cell. The eight selected interfaces, confined within 576-atom limit, and 10% mean absolute strain, are highlighted in different colors.

where *a* is lattice constant—and number of atoms in the unit cell of the heterostructures.

In the current study, a systematic approach was employed to select the interfaces, ensuring that the strain remained within a limit of 10%, while also maintaining computational feasibility (total number of atoms ≤ 576). As shown in Figure 1, this criterion resulted in eight distinct interfaces for subsequent analysis. A detailed numerical analysis of the strain present at the selected interfaces is outlined in Table 1.

From the geometrical standpoint, the main connecting points between the two materials are the outermost oxygen atoms, which is a standard bridging mechanism for metal oxides. On the $TiO_2(101)$ surface, there are the undercoordinated topmost surface O atoms and subsurface Ti atoms, while on the $Cu_2O(111)$ surface, there are subsurface undercoordinated Cu atoms present in the same plane with coordinatively saturated Cu atoms linking two O atoms, while the topmost surface O atoms are undercoordinated. However, due to the approximately 2:1 ratio of available Ti to Cu atoms (per unit cell or comparable surface area) as well as $O^{top}_{TiO_2}$ to $O^{top}_{Cu_2O}$ atoms, it is to be expected that a certain number of bonds will remain undercoordinated.

Upon relaxation, the TiO_2 topmost 2-fold coordinated O atoms formed a bond at the interface with the singly coordinated Cu atoms on the Cu_2O side and the 3-fold coordinated O atoms from the Cu_2O side bonded with the 5-fold undercoordinated titanium atoms from TiO_2. However, depending on the amount of lateral and shear strain present in the initial model, the number of formed bonds differs greatly among the eight chosen interfaces. This can be observed in the calculated adhesive energy, listed in Table 1, which is a direct quantity (at the computational level) allowing one to evaluate the probability of observing the corresponding epitaxial interface. From the computed values, it is notable that not all interfacial structures result in equal energy gains once the interface is formed.

The energetically most stable interface is found to be interface 2, which is shown in Figure 2. This interface has the lowest amount of lateral strain (present in the film) while at the same time undergoing no shear strain. In this configuration, all of the O atoms from the substrate and film are coordinatively saturated upon relaxation (completion of their octet), while every other Ti atom remains undercoordinated.

The accurate assessment of band bending properties at interfaces requires a comprehensive understanding of the structural and electronic changes induced by the formation of the interface. The independent slab approximation only provides an incomplete representation of the band alignment, resulting in significant discrepancies when compared to experimental data.[77] Explicit interfacial relaxations can induce a shift in the band alignment as much as 130 meV highlighting the key role of the relaxation in the precise estimation of band alignment.[78] The relaxed structures of interfaces 1−8 are shown in Figure S3.

Band Alignment. When two semiconductor materials form an interface, a discontinuity in their band edges occurs. In the computational evaluation of these relative band edges, a challenge arises due to the absence of an absolute reference energy in an infinite solid attributed to the long-range nature of the columbic interaction.[79] To address this, the average electrostatic potential has been suggested as a consistent energy reference in such systems.[80,81] The method involves first determining the average of the electrostatic potential of the interface followed by calculating the band edges of the individual slabs relative to their average electrostatic potential for the individual slabs. It is crucial to account for the strain induced by interfacial relaxations; therefore, the relaxed slab geometries should be utilized in these calculations without further relaxations.[82]

Functional. Within the framework of DFT, generalized gradient approximation (GGA) functionals suffer from self-interaction errors, which result in the systematic underestimation of band gaps and the overestimation of cohesive energies in materials.[83] To address these limitations, hybrid functionals, which integrate a mix of Fock exchange with semilocal exchange, are designed to mitigate this delocalization

Table 1. Details of the Strain Matrices in the Supercell of the Selected Interfaces and Corresponding Adhesive and Interface Energies, Where ε_{xx} and ε_{yy} are the Normal Strains along the *x* and *y* Directions and ε_{xy} Represents the Shear Strain in the *x*−*y* Plane

interface	ε_{xx} (%)	ε_{yy} (%)	ε_{xy} (%)	mean absolute strain (%)	Adhesive en. β (J/m^2)	Interface en. γ (J/m^2)
1	5.87	−1.39	0.00	2.42	2.29	−0.13
2	4.59	−1.39	0.00	2.03	2.94	−0.95
3	3.12	0.01	−2.55	1.89	1.41	0.48
4	−5.15	−2.14	−1.66	2.98	2.03	0.04
5	−5.13	4.36	−2.74	4.07	1.48	0.53
6	−9.02	2.02	7.52	6.19	1.90	1.16
7	−14.60	8.69	0.00	7.76	1.43	1.82
8	5.05	−5.76	−0.88	3.90	1.27	0.48

https://doi.org/10.1021/acsami.4c06081
ACS Appl. Mater. Interfaces 2024, 16, 35781−35792

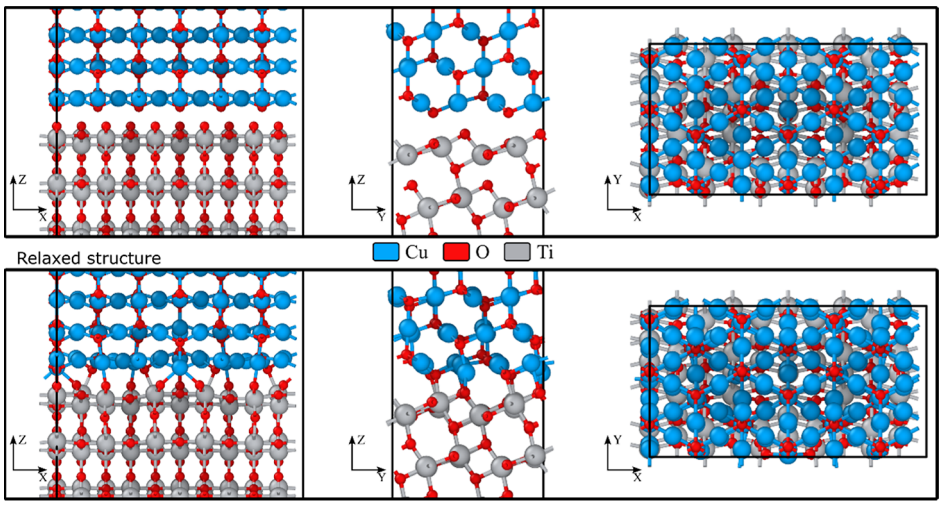

Figure 2. Initial and relaxed atomic structure of the most stable Cu_2O/TiO_2 interface 2, viewed along all three crystallographic axes. Vacuum is present along the *Z*-axis, but it is omitted for clarity.

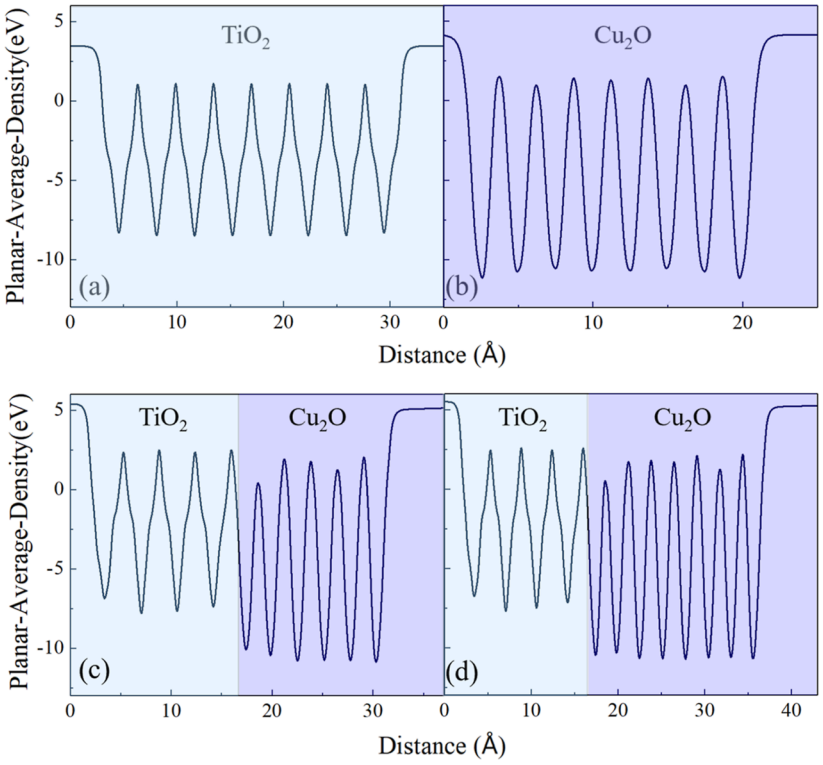

Figure 3. Thickness assessment of interface 1 in relation to the thickness of the Cu_2O through planar-averaged electrostatic potential: (a,b) independent slab approximation (before contact). (c) Explicit interface of Cu_2O/TiO_2 with 6 layers of Cu_2O and (d) 8 layers of Cu_2O.

error.[84] The partial incorporation of the exact exchange from the Hartree−Fock theory into these functionals helps to correct the self-interaction error, thereby providing a more accurate representation of electron correlation and localization. This adjustment is crucial for electronic properties, as it leads to a more precise prediction of band gaps. However, hybrid functionals are computationally demanding, and the relaxation of the heterostructures comprising hundreds of atoms becomes impractical. Consequently, a synergic approach that combines the computational efficiency of GGA functionals with the accuracy of the hybrid functionals can be employed. This combined approach enables an accurate assessment of the band bending at a reasonable computational cost. It consists of heterostructure relaxation via GGA functionals and assessment of the band edge positions of isolated slabs via hybrid functionals.

In calculating the band alignment, since the average electrostatic potential is a function of the ground state charge density and the difference in the distribution of electronic density obtained with different functionals, which determines the Hartree potential, is small,[85] the potential lineup can be accurately determined via GGA[86,87] and many-body corrections[88] or hybrid functionals such as PBE0 schemes[78] can barely affect the band potential lineup in accordance with findings for semiconductor−insulator interfaces.[87] For instance, it has been shown that the potential alignments

https://doi.org/10.1021/acsami.4c06081
ACS Appl. Mater. Interfaces 2024, 16, 35781−35792

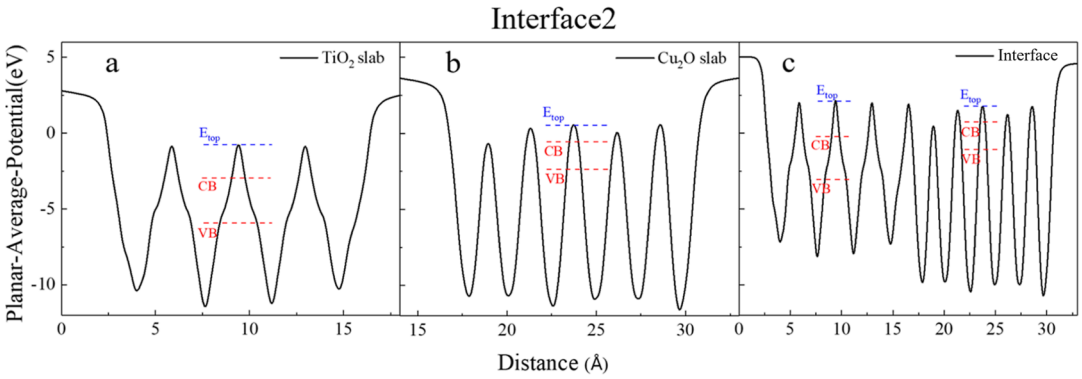

Figure 4. Planar-averaged electrostatic potentials in the $x-y$ plane of (a,b) the isolated slabs with the interface geometries and (c) of interface 2 as a function of the distance along the z-direction, normal to the interface. E_{top} denotes the reference energy, and the CB and VB edges in the interface are aligned based on their respective values to the E_{top} in the isolated slabs' calculations.

calculated within the GGA are in agreement with those calculated using HSE to within 50 meV, despite the GGA calculations being 10−100 times less computationally expensive.[89] Other hybrid functional studies of Si and TiO_2 surfaces[90] and a self-consistent GW study of a Si/SiO_2 interface[83] have indeed shown that the changes in the averaged electrostatic potential from the semilocal values are less than 0.1 eV at these surfaces and interface. Moreover, the functional dependence of the formation energies of Si self-interstitials as a function of the electronic chemical potential has shown that taking the average electrostatic potential as the reference of the energy results in invariant features in the formation energy for any given value of chemical potential.[85] Thus, considering the accuracy of potential alignments via GGA, they can be combined with hybrid calculations of the isolated slabs' band structure toward accurate band alignments with a high computational efficiency.[89]

While GGA calculations present a lower computational cost compared with more sophisticated methods, the computational demands still escalate significantly for large-scale systems. Therefore, it is imperative to employ the minimal slab thicknesses and thus the lowest possible number of atoms in the calculations. This reduction in system size in justified by the localized nature of interfacial electronic properties at neutral interfaces.[86] The interfacial properties are usually confined within a few atomic units from the interface beyond where the bulk properties of charge density rapidly converge. To consider the smallest possible interface and verify the assessment of the slab thicknesses via surface energy (Figure S2), the average electrostatic potential of interface 1 is calculated in comparison to the independent slabs' approximation in Figure 3. Since TiO_2 is the substrate and does not undergo strain (only chemical alterations at the interface itself), its electrostatic potential, as shown in Figure 3a, remains relatively unchanged when compared with the explicit interfaces depicted in Figure 3c,d. In contrast, due to the imposed strain on Cu_2O, it is more influenced by the interfacial effects, which only penetrate no more than two atomic layers from the interface, as can be seen in Figure 3c. To validate the sufficiency of the 6-layer Cu_2O slab, an 8-layer slab is also examined in Figure 3d, which reveals a continuation of the bulk-like behavior within the central layers of the slab. This finding suggests that the 6-layer Cu_2O slab adequately captures the intrinsic electrostatic characteristics of the bulk. Consequently, the Cu_2O(6-layer)/TiO_2 (4-layer) model configuration is selected throughout this study.

As mentioned above, an electrostatic potential approach has been employed to assess the band bending of the various interfaces. This method entails calculating the electrostatic potential, averaged across the $x-y$ plane. The resulting data for interface 2 is depicted in Figure 4, where the planar-averaged electrostatic potential is plotted as a function of the distance along the z-axis, normal to the interface plane. Notably, this profile shows distinct minima corresponding to atomic planes, indicating areas with a higher electron density. In the section of the interface composed of TiO_2 Figure 4a, notable deviations are observed in the potential profile. These deviations are attributed to the displacement of the O atoms relative to the Ti-containing planes, a structural feature inherent to the anatase phase of TiO_2. This atomic arrangement results in characteristic "shoulders" in the potential curve, observable throughout the entire extent of the anatase layer.

When determining an appropriate reference point on the electrostatic potential curve, concerns arise regarding the precision of planar-averaged potentials at planes containing atoms. The main challenge comes from the necessity to integrate the electrostatic potential in the proximity of atomic positions, where the potential changes very quickly and sharply. These steep variations in potential make it difficult to compute the potential accurately, particularly over confined regions, such as within a single lattice period. To address this issue, as outlined by Conesa,[81] in this study, instead of relying on the planar-averaged potential at the atom-containing planes, we utilized the energy value at the point of zero slope (termed E_{top}). These zero-slope points typically occur near the midpoint between successive atomic planes. This method is considered to be more reliable for determining the reference value for electronic levels. The analysis reveals that these zero slope values display oscillations within each slab near the interface, but they stabilize to a constant value toward the center of each slab. The resultant values for interface 2 are E_{top} = 2.11 and 1.79 eV for the TiO_2 and Cu_2O regions, respectively.

After the reference energies (E_{top}), the next step is determining the band edges of the individual slabs relative to these reference energies. To achieve this, the planar-averaged electrostatic potential was computed for the individual TiO_2 and Cu_2O slabs. However, it is important to note that the slabs acting as films are distorted due to epitaxial strain, and to accurately represent the electronic properties under these conditions, it is imperative to calculate the electrostatic potentials for the distorted structures. Thus, hybrid functional

https://doi.org/10.1021/acsami.4c06081
ACS Appl. Mater. Interfaces 2024, 16, 35781−35792

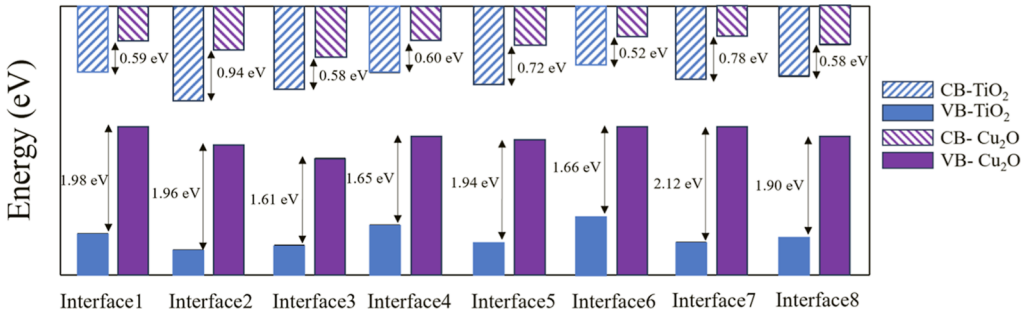

Figure 5. Summary of the band alignment results for interfaces 1−8. The band offsets, ΔE_v and ΔE_c, are indicated for each interface.

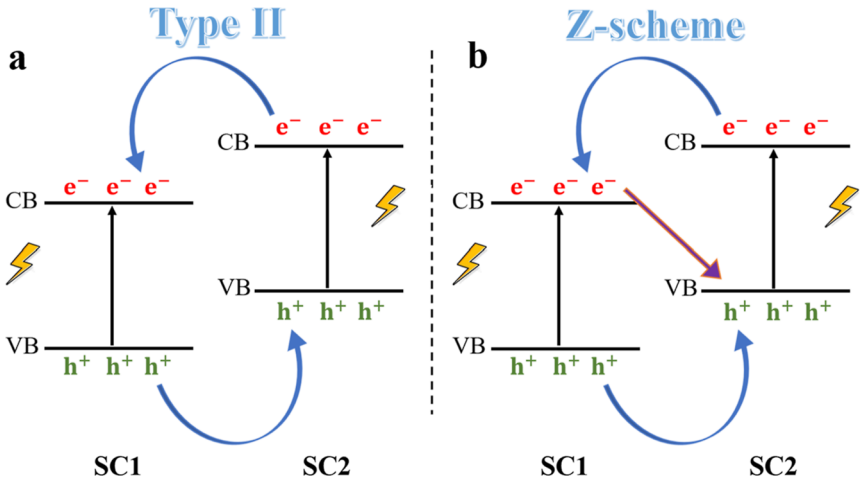

Figure 6. Schematic illustration of charge transfer mechanism after light illumination. (a) Type II, where electrons and holes transfer in an antiparallel way, and (b) *Z*-scheme, where after the antiparallel charge transfer, electrons in SC1 combine with the holes in SC2 (SC stands for semiconductor).

calculations were performed, considering the distorted slab structures as they exist at the interface without any further relaxations. Figure 4a,b shows the results of the hybrid calculation for the individual TiO_2 and Cu_2O, respectively, where the relative positions of the VB and CB edges are shown with respect to the E_{top} for each slab. With the band edges of both materials positioned relative to the reference energy, the final band offsets are conclusively determined and are depicted in Figure 4c. The findings suggest a staggered-type alignment at the interface, wherein the band edges of Cu_2O are positioned at a higher energy level compared to those of TiO_2. Similar results are obtained for the other interfaces, and the details are presented in Figures S4−S10. The band alignment results for all the interfaces are summarized in Figure 6. This figure highlights the variations in the positions of the VB and CB edges across different interfaces as a result of their different interfacial morphologies. Despite these variations, a key observation is the consistent presence of a staggered-type alignment across all of the interfaces. The values of the band offsets, as noted in the graph, are comparable to the experimental values of ΔE_v = 1.93 eV,[91] 1.71 eV,[92] ΔE_c = 0.81 eV,[91] and 0.88 eV.[92] This uniformity in the alignment type, despite differences in the specific energy levels of the band edges, underscores a fundamental characteristic of these heterojunctions.

For comparison, we computed the valence and CB offsets in the independent compound approximation and through the averaged electrostatic potential method (results listed in Tables S1 and S2). The computed IP and EA of TiO_2 and Cu_2O compare well with experimental values; however, the band offsets are overestimated in this approach. When employing the macroscopic averaging technique of the interface electrostatic potential to obtain the offset in the potential across the interface, the results (1.93 eV for VBO and 0.42 eV for CBO) compare much closer to the measured experimental values. This confirms once again how indispensable explicit modeling of interfacial structures is for accurate electronic band behavior at junctions.

While band alignment configurations provide valuable insights into the arrangement of band edges at the interface, they do not conclusively establish the charge transfer properties. Specifically, as illustrated in Figure 6, within a staggered-type alignment between two semiconductors (SC1 and SC2), there exist two possible configurations for charge transfer. Figure 6a depicts a type II configuration wherein charge separation is achieved via the antiparallel transfer of photoexcited electrons and holes in the opposite direction. Whereas Figure 6b depicts a scenario where the photoexcited electrons in SC2 recombine with the holes in SC1 through a *Z*-scheme mechanism.

Hence, to differentiate between type II and *Z*-scheme charge transfer mechanisms, it is essential to quantify the charge density difference at the interfaces, defined as

$$\Delta\rho = \rho_{\text{interface}} - \rho_{TiO_2} - \rho_{Cu_2O} \tag{2a}$$

where $\Delta\rho$ is the charge density difference at the interface, $\rho_{\text{interface}}$ is the charge density of the interface, and ρ_{TiO_2} and

https://doi.org/10.1021/acsami.4c06081
ACS Appl. Mater. Interfaces 2024, 16, 35781−35792

ρ_{Cu_2O} are the charge densities of the corresponding slabs before contact.

Figure 7 shows $\Delta\rho$ for interface 2 where the dashed line represents the midpoint layer of the interface. The figure

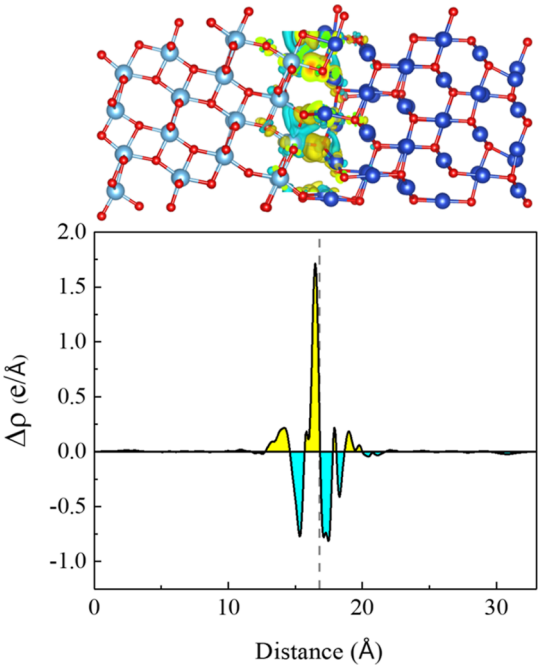

Figure 7. Charge density difference of interface 2. Yellow: charge accumulation. Cyan: charge depletion. The dashed line represents the midpoint layer of the interface. Isosurface value is set to 0.0015 for the orbital visualization.

suggests a directional charge transfer toward the interface from both the Cu_2O and TiO_2 layers. However, a closer inspection of the structure reveals that the electrons are transferred from the transition metal toward the oxygen. That is nothing else than the bond formation process confirmed which was discussed when the adhesion energies were discussed. The two charge depletion regions in Figure 7 are approximately half the value of the main charge accumulation region at the interface. In addition, we computed the electron dipole moment at the interface. A maximal value of 0.1 D was obtained, arising from the disparity between the number of metal ions present to form bonds at the interface (see discussion of structure at the interface), which offers space for band bending to occur.

The charge density difference for all other interfaces is presented in Figures S11−S17. A consistent pattern of charge transfer between the transition metal and the interface oxygen is found across all interfaces. However, one should treat these results with care as they have been computed with a semilocal functional, thus not entirely circumventing the well-known charge delocalization error for d-electron-bearing transition metals, which can affect the value of the interface dipole and corresponding charge transfer.

To further verify the charge transfer direction, we evaluated the Fermi energies (E_F) before and after contact. When two semiconductors with different Fermi energies come into contact, charge transfer occurs from the material with the higher E_F to the one with the lower E_F until the Fermi levels equilibrate. Figure 8c shows the E_F of interface 2 in comparison with the E_F of the individual slabs before contact (Figure 8a,b). It is evident that Cu_2O has a higher E_F compared to that of TiO_2. Consequently, upon contact in the interface, charges transfer from Cu_2O to TiO_2 until the Fermi levels reach equilibrium. This charge transfer direction is consistent with the charge depletion observed in Cu_2O and charge accumulation in TiO_2, as seen in Figure 7. The Fermi energy assessment for other interfaces is shown in Figures S18−S24. The findings suggest the same charge transfer mechanism across all of the interfaces.

The comprehensive analysis of charge transfer mechanisms in Figures 4, 5, 7, and 8, leads to the proposal of distinct behavior under visible and ultraviolet light illumination, specifically focusing on the photocatalytic behavior of the Cu_2O/TiO_2 interface. As shown in Figure 9a, under visible light, only Cu_2O would be photoexcited due to its suitable band gap. This could potentially result in the generation of photoexcited electrons and holes within Cu_2O. However, the band bending configuration at the interface, given the charge depletion and accumulation in Cu_2O and TiO_2, respectively, causes the Cu_2O bands to bend upward and TiO_2 to bend downward, forming a *Z*-scheme band bending configuration. In this configuration, the photoexcited electrons in Cu_2O would encounter an energy barrier that hinders their transfer to TiO_2. Consequently, these photoexcited electrons and holes are unable to separate efficiently, leading to their recombination within the Cu_2O material. This recombination typically occurs on a very fast time scale (femtosecond to picosecond), which is much quicker than the time scale of chemical

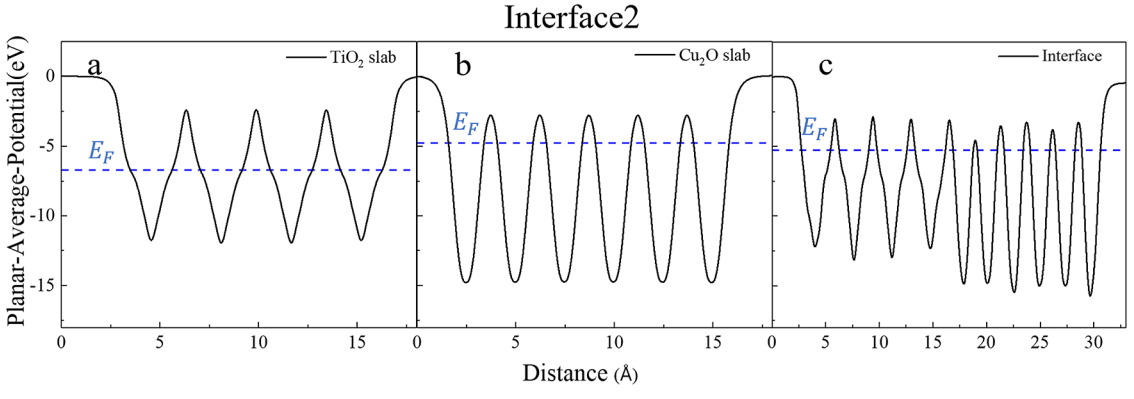

Figure 8. Fermi energy assessment of interface 2 (a,b) before and (c) after contact.

https://doi.org/10.1021/acsami.4c06081
ACS Appl. Mater. Interfaces 2024, 16, 35781−35792

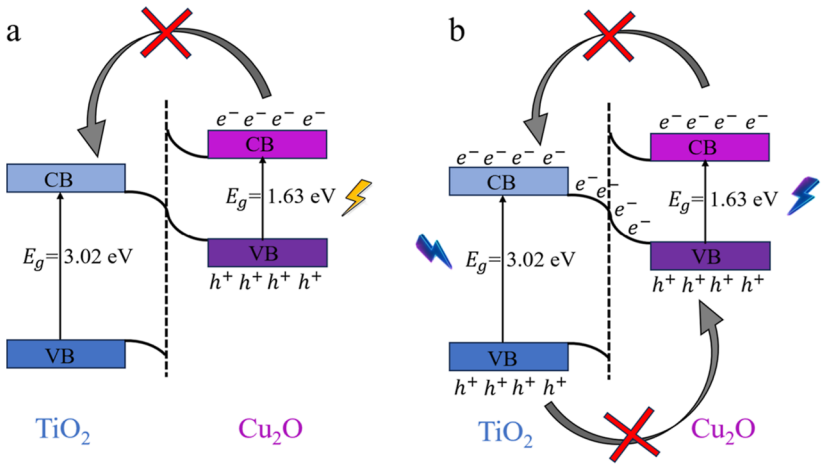

Figure 9. Proposed band bending configuration for Cu_2O/TiO_2 interfaces under (a) visible and (b) ultraviolet light illumination.

reactions (milliseconds).[93] As a result, these carriers recombine before they can participate in photocatalytic reactions, leading to a reduced photocatalytic activity under visible light.

In contrast, under ultraviolet or violet light illumination, both Cu_2O and TiO_2 are excited. In this scenario, the *Z*-scheme band bending plays a pivotal role in dictating the charge transfer dynamics. Specifically, the photoexcited electrons from TiO_2 recombine with the photoexcited holes in Cu_2O. This recombination process effectively separates the photoexcited holes in TiO_2 from the photoexcited electrons in Cu_2O. The separated charge carriers—photoexcited holes on TiO_2 and photoexcited electrons on Cu_2O—are now available to participate in photocatalytic chemical reactions. This separation enhances the photocatalytic efficiency under ultraviolet light as the carriers are able to participate in redox reactions. This observed *Z*-scheme band alignment configuration is consistent with numerous experimental investigations that have analyzed similar crystal facets, specifically TiO_2 (101) and Cu_2O(111).[94,95]

CONCLUSIONS

In conclusion, this study delves into the intricate interplay among interfacial morphologies, band bending effects, and charge transfer dynamics in anatase Cu_2O/TiO_2 epitaxial heterostructures for photocatalytic applications. Through a systematic exploration, starting from well-defined TiO_2 (101) and Cu_2O(111) slab structures, explicit epitaxial heterojunctions where TiO_2 serves as a substrate for a Cu_2O film were created. Out of the obtained structures, those with a lattice mismatch of less than 10% were selected for further optimization. Eight distinct interfaces were identified, all with consistent staggered-type band alignment, providing valuable insights into the fundamental characteristics of these heterojunctions.

Despite variations in band edge positions, a systematic charge transfer from Cu_2O to TiO_2 was observed across all of the interfaces. The proposed band bending can help explain the nuances of charge separation at the Cu_2O/TiO_2 interface, as evidenced in earlier experiments. The observed *Z*-scheme band alignment under ultraviolet light aligns with experimental investigations, highlighting its relevance to enhancing photocatalytic efficiency. This theoretical investigation contributes to the understanding of the structural and electronic factors influencing the photocatalytic behavior of heterostructures, paving the way for the rational design and optimization of photocatalytic materials for environmental remediation applications.

It is essential to recognize that the experimental processes inherently introduce defects and impurities that can significantly influence the band bending properties of interfaces. Future research should therefore be directed toward a detailed investigation of how these unavoidable imperfections affect the electronic structure of the interfaces. This entails a systematic study of the type and concentrations of defects and impurities as well as their spatial distribution within the material. Additionally, it is crucial to explore the mechanisms through which these defects and impurities interact with materials' electronic states. Such studies are vital for advancing our theoretical understanding of the interfaces and providing directions for experimental studies.

ASSOCIATED CONTENT

Supporting Information

The Supporting Information is available free of charge at https://pubs.acs.org/doi/10.1021/acsami.4c06081.

Slab morphologies of the 4-bilayer TiO_2 (101) surface and 6-trilayer Cu_2O(111) surface; surface energy convergence; relaxed structure of Cu_2O/TiO_2 interfaces; computed values of the electronic band gap, IP, EA, band offsets at the Cu_2O/TiO_2 interface; planar-averaged electrostatic potentials; charge density difference across individual interfaces; and Fermi energy assessment across Cu_2O/TiO_2 interfaces (PDF)

AUTHOR INFORMATION

Corresponding Authors

Aleksandar Živković − *Department of Earth Sciences, Utrecht University, 3548CB Utrecht, The Netherlands; Institute of Inorganic Chemistry, Christian-Albrecht University of Kiel, 24118 Kiel, Germany;* orcid.org/0000-0003-1347-6203; Email: a.zivkovic@uu.nl

Steven P. Lewis − *Department of Physics and Astronomy, University of Georgia, Athens, Georgia 30602, United States*; Email: splewis@uga.edu

https://doi.org/10.1021/acsami.4c06081
ACS Appl. Mater. Interfaces 2024, 16, 35781−35792

Authors

Mona Asadinamin − *Department of Physics and Astronomy, University of Georgia, Athens, Georgia 30602, United States;* orcid.org/0000-0002-4651-044X

Nora H. de Leeuw − *Department of Earth Sciences, Utrecht University, 3548CB Utrecht, The Netherlands; School of Chemistry, University of Leeds, LS2 9JT Leeds, U.K.;* orcid.org/0000-0002-8271-0545

Complete contact information is available at: https://pubs.acs.org/10.1021/acsami.4c06081

Notes

The authors declare no competing financial interest.

■ ACKNOWLEDGMENTS

A.Ž. and N.H.D.L. acknowledge the NWO ECHO grant (712.018.005) for funding.

■ REFERENCES

(1) Yan, J.; Wu, H.; Chen, H.; Zhang, Y.; Zhang, F.; Liu, S. F. Fabrication of TiO2/C3N4 heterostructure for enhanced photocatalytic Z-scheme overall water splitting. *Appl. Catal., B* **2016**, *191*, 130−137.

(2) Jeon, N. J.; Noh, J. H.; Kim, Y. C.; Yang, W. S.; Ryu, S.; Seok, S. I. Solvent engineering for high-performance inorganic-organic hybrid perovskite solar cells. *Nat. Mater.* **2014**, *13* (9), 897−903.

(3) Malinkiewicz, O.; Yella, A.; Lee, Y.; Espallargas, G.; Graetzel, M.; Nazeeruddin, M.; Bolink, H. Perovskite solar cells employing organic charge-transport layers. *Nat. Photonics* **2014**, *8* (2), 128−132.

(4) Huang, J.; Yuan, Y.; Shao, Y.; Yan, Y. Understanding the physical properties of hybrid perovskites for photovoltaic applications. *Nat. Rev. Mater.* **2017**, *2* (7), 17042.

(5) Dong, S.; Feng, J.; Fan, M.; Pi, Y.; Hu, L.; Han, X.; Liu, M.; Sun, J.; Sun, J. Recent developments in heterogeneous photocatalytic water treatment using visible light-responsive photocatalysts: a review. *RSC Adv.* **2015**, *5* (19), 14610−14630.

(6) Li, A.; Wang, Z.; Yin, H.; Wang, S.; Yan, P.; Huang, B.; Wang, X.; Li, R.; Zong, X.; Han, H.; Li, C. Understanding the anatase-rutile phase junction in charge separation and transfer in a TiO2 electrode for photoelectrochemical water splitting. *Chem. Sci.* **2016**, *7* (9), 6076−6082.

(7) Zhang, Z.; Yates, J. T., Jr. Band bending in semiconductors: chemical and physical consequences at surfaces and interfaces. *Chem. Rev.* **2012**, *112* (10), 5520−5551.

(8) Ihn, T. *Semiconductor Nanostructures: Quantum States and Electronic Transport*; Oxford University Press, 2009.

(9) Huang, M. H.; Madasu, M. Facet-dependent and interfacial plane-related photocatalytic behaviors of semiconductor nanocrystals and heterostructures. *Nano Today* **2019**, *28*, 100768.

(10) Kubyshkina, E.; Unge, M. Impact of interfacial structure on the charge dynamics in nanocomposite dielectrics. *J. Appl. Phys.* **2019**, *125* (4), 045109.

(11) Ramana, C. V.; Makeswaran, N.; Zade, V.; Das, D.; Tan, S.; Xu, S.; Beyerlein, I. J. Fabrication and Characterization of High-Quality Epitaxial Nanocolumnar Niobium Films with Abrupt Interfaces on YSZ(001). *J. Phys. Chem. C* **2022**, *126* (4), 2098−2107.

(12) Ohtake, A.; Yang, X. Fabrication of Lattice-Mismatched MoTe2/MoSe2 Heterostructures using Molecular-Beam Epitaxy. *Cryst. Growth Des.* **2023**, *23* (7), 5001−5007.

(13) Osbourn, G. C. Strained-layer superlattices from lattice mismatched materials. *J. Appl. Phys.* **1982**, *53* (3), 1586−1589.

(14) Ostheim, L.; Klar, P. J.; Moryson, Y.; Rohnke, M.; Beyer, A.; Volk, M.; Munde, M.; Stolz, W.; Volz, K. Effect of the interface morphology on the lateral electron transport in (001) GaP/Si heterostructures. *J. Appl. Phys.* **2019**, *126* (21), 215704.

(15) Baniecki, J. D.; Yamazaki, T.; Ricinschi, D.; Van Overmeere, Q.; Aso, H.; Miyata, Y.; Yamada, H.; Fujimura, N.; Maran, R.; Anazawa, T.; et al. Strain Dependent Electronic Structure and Band Offset Tuning at Heterointerfaces of ASnO3 (A = Ca, Sr, and Ba) and SrTiO3. *Sci. Rep.* **2017**, *7* (1), 41725.

(16) Clavel, M. B.; Hudait, M. K. Band Offset Enhancement of a-Al2O3/Tensile-Ge for High Mobility Nanoscale pMOS Devices. *IEEE Electron Device Lett.* **2017**, *38* (9), 1196−1199.

(17) Lian, S.; Wu, H.; Wu, P.; Sun, H.; An, Y. Strain and interfacial defect tailored electronic structures of two-dimensional WSe2/h-BN van der Waals heterostructure. *Int. J. Mod. Phys. B* **2023**, *37* (31), 2350277.

(18) Park, J.-S.; Jung, Y.-K.; Butler, K. T.; Walsh, A. Quick-start guide for first-principles modelling of semiconductor interfaces. *J. Phys.: Energy* **2018**, *1* (1), 016001.

(19) Demkowicz, M. J.; Wang, J.; Hoagland, R. G. Interfaces Between Dissimilar Crystalline Solids. In *Dislocations in Solids*; Hirth, J. P., Ed.; Vol. *14*; Elsevier, 2008; pp 141−205.

(20) Herbig, M.; Choi, P.; Raabe, D. Combining structural and chemical information at the nanometer scale by correlative transmission electron microscopy and atom probe tomography. *Ultramicroscopy* **2015**, *153*, 32−39.

(21) Ruan, Y. C.; Ching, W. Y. An effective dipole model for predicting band offsets in semiconductor heterojunctions. *J. Appl. Phys.* **1986**, *60* (11), 4035−4038.

(22) Akinci, Ö.; Gürel, H. H.; Ünlü, H. Semi-empirical tight binding modelling of CdSTe/CdTe, ZnSSe/ZnSe and ZnSSe/CdSe heterostructures. *Thin Solid Films* **2009**, *517* (7), 2431−2437.

(23) Zhou, Y.-D.; Zhao, Z.-Y. Interfacial structure and properties of TiO2 phase junction studied by DFT calculations. *Appl. Surf. Sci.* **2019**, *485*, 8−21.

(24) Živković, A.; Mallia, G.; King, H. E.; de Leeuw, N. H.; Harrison, N. M. Mind the Interface Gap: Exposing Hidden Interface Defects at the Epitaxial Heterostructure between CuO and Cu2O. *ACS Appl. Mater. Interfaces* **2022**, *14* (50), 56331−56343.

(25) Di Liberto, G.; Tosoni, S.; Pacchioni, G. Z-Scheme versus type-II junction in g-C3N4/TiO2 and g-C3N4/SrTiO3/TiO2 heterostructures. *Catal. Sci. Technol.* **2021**, *11* (10), 3589−3598.

(26) Hou, Y.; Li, X. Y.; Zhao, Q. D.; Quan, X.; Chen, G. H. Fabrication of Cu2O/TiO2 nanotube heterojunction arrays and investigation of its photoelectrochemical behavior. *Appl. Phys. Lett.* **2009**, *95* (9), 093108.

(27) Wang, Y.; Tao, J.; Wang, X.; Wang, Z.; Zhang, M.; He, G.; Sun, Z. A unique Cu2O/TiO2 nanocomposite with enhanced photocatalytic performance under visible light irradiation. *Ceram. Int.* **2017**, *43* (6), 4866−4872.

(28) Liu, Z.; Yan, L. High-efficiency p−n junction oxide photoelectrodes for photoelectrochemical water splitting. *Phys. Chem. Chem. Phys.* **2016**, *18* (45), 31230−31237.

(29) Sharma, M.; Mandal, M. K.; Pandey, S.; Kumar, R.; Dubey, K. K. Visible-Light-Driven Photocatalytic Degradation of Tetracycline Using Heterostructured Cu2O-TiO2 Nanotubes, Kinetics, and Toxicity Evaluation of Degraded Products on Cell Lines. *ACS Omega* **2022**, *7* (37), 33572−33586.

(30) Li, R.; Zhang, R.; Qiao, Y.; Zhang, D.; Cui, Z.; Wang, W. Heterostructure Ni(OH)2/ZrO2 catalyst can achieve efficient oxygen reduction reaction. *Chem. Eng. Sci.* **2022**, *250*, 117398.

(31) Andrade, A. O. C.; Lacerda, L. H. d. S.; Lage Júnior, M.; Sharma, S. K.; Maia da Costa, M. E. H.; Alves, O. C.; Santos, E. C. S.; dos Santos, C. C.; de Menezes, A. S.; San-Miguel, M. A.; et al. Enhanced photocatalytic activity of BiOBr/ZnWO4 heterojunction: A combined experimental and DFT-based theoretical approach. *Opt. Mater.* **2023**, *138*, 113701.

(32) Yu, W.; Gui, Q.; Wan, X.; Robertson, J.; Zhang, Z.; Guo, Y. High-throughput interface prediction and generation scheme: The case of β-Ga2O3/AlN interfaces. *Appl. Phys. Lett.* **2023**, *123* (16), 161601.

(33) Zhang, Q.; Zhang, H.; Gu, B.; Tang, Q.; Cao, Q.; Fang, W. Sunlight-driven photocatalytic oxidation of 5-hydroxymethylfurfural over a cuprous oxide-anatase heterostructure in aqueous phase. *Appl. Catal., B* **2023**, *320*, 122006.

(34) Schneider, J.; Matsuoka, M.; Takeuchi, M.; Zhang, J.; Horiuchi, Y.; Anpo, M.; Bahnemann, D. W. Understanding TiO2 Photocatalysis: Mechanisms and Materials. *Chem. Rev.* **2014**, *114* (19), 9919−9986.
(35) Hara, M.; Kondo, T.; Komoda, M.; Ikeda, S. N.; Kondo, J.; Domen, K.; Hara, M.; Shinohara, K.; Tanaka, A. Cu2O as a photocatalyst for overall water splitting under visible light irradiation. *Chem. Commun.* **1998**, No. 3, 357−358.
(36) Wang, M.; Sun, L.; Lin, Z.; Cai, J.; Xie, K.; Lin, C. p-n Heterojunction photoelectrodes composed of Cu2O-loaded TiO2 nanotube arrays with enhanced photoelectrochemical and photoelectrocatalytic activities. *Energy Environ. Sci.* **2013**, *6* (4), 1211−1220.
(37) Nair, R. V.; Gummaluri, V. S.; Matham, M. V.; C, V. A review on optical bandgap engineering in TiO2 nanostructures via doping and intrinsic vacancy modulation towards visible light applications. *J. Phys. D: Appl. Phys.* **2022**, *55* (31), 313003.
(38) Pagare, P. K.; Torane, A. Band gap varied cuprous oxide (Cu 2 O) thin films as a tool for glucose sensing. *Microchim. Acta* **2016**, *183*, 2983−2989.
(39) Tamirat, A. G.; Rick, J.; Dubale, A. A.; Su, W.-N.; Hwang, B.-J. Using hematite for photoelectrochemical water splitting: a review of current progress and challenges. *Nanoscale Horiz.* **2016**, *1* (4), 243−267.
(40) Durgalakshmi, D.; Ajay Rakkesh, R.; Rajendran, S.; Naushad, M. Principles and Mechanisms of Green Photocatalysis. In *Green Photocatalysts*; Naushad, M., Rajendran, S., Lichtfouse, E., Eds.; Springer International Publishing, 2020; pp 1−24.
(41) Cosma, D.; Urda, A.; Radu, T.; Rosu, M. C.; Mihet, M.; Socaci, C. Evaluation of the Photocatalytic Properties of Copper Oxides/Graphene/TiO2 Nanoparticles Composites. *Molecules* **2022**, *27* (18), 5803.
(42) Sun, L.; Han, L.; Li, N.; Wang, P.; Wang, M.; Luo, X.; Li, X. P25-induced polydopamine conformal assembly on Cu2O polyhedra for hydrophilic and stable photoelectrochemical performance. *J. Mater. Chem. C* **2022**, *10* (38), 14194−14201.
(43) Cheng, S.-P.; Wei, L.-W.; Wang, H.-P. Photocatalytic Reduction of CO2 to Methanol by Cu2O/TiO2 Heterojunctions. *Sustainability* **2021**, *14* (1), 374.
(44) Hou, R.; Jia, Y.; Jin, G.; Shi, M.; Jiang, N. Enhanced photocatalytic performance of Cu2O/TiO2/rGA composites to degrade gas-phase unsymmetrical dimethylhydrazine. *J. Mater. Sci.* **2022**, *57* (5), 3538−3552.
(45) Wang, S.; Kavaipatti, B.; Kim, S.-J.; Pan, X.; Ramesh, R.; Ager, J. W., III; Wang, L.-W. Atomic and electronic structures of lattice mismatched Cu2O/TiO2 interfaces. *Appl. Phys. Lett.* **2014**, *104* (21), 211605.
(46) Nie, J.; Yu, X.; Hu, D.; Wang, T.; Liu, Z.; Zhao, N.; Li, J.; Yao, B. Preparation and Properties of Cu2O/TiO2 Heterojunction Nanocomposite for Rhodamine B Degradation under Visible Light. *ChemistrySelect* **2020**, *5* (27), 8118−8128.
(47) Seidl, A.; Görling, A.; Vogl, P.; Majewski, J. A.; Levy, M. Generalized Kohn-Sham schemes and the band-gap problem. *Phys. Rev. B: Condens. Matter Mater. Phys.* **1996**, *53* (7), 3764−3774.
(48) Kresse, G.; Furthmüller, J. Efficient iterative schemes for ab initio total-energy calculations using a plane-wave basis set. *Phys. Rev. B: Condens. Matter Mater. Phys.* **1996**, *54* (16), 11169−11186.
(49) Kresse, G.; Joubert, D. From ultrasoft pseudopotentials to the projector augmented-wave method. *Phys. Rev. B: Condens. Matter Mater. Phys.* **1999**, *59* (3), 1758−1775.
(50) Perdew, J. P.; Burke, K.; Ernzerhof, M. Generalized gradient approximation made simple. *Phys. Rev. Lett.* **1996**, *77* (18), 3865−3868.
(51) Ernzerhof, M.; Scuseria, G. E. Assessment of the Perdew-Burke-Ernzerhof exchange-correlation functional. *J. Chem. Phys.* **1999**, *110* (11), 5029−5036.
(52) Krukau, A. V.; Vydrov, O. A.; Izmaylov, A. F.; Scuseria, G. E. Influence of the exchange screening parameter on the performance of screened hybrid functionals. *J. Chem. Phys.* **2006**, *125* (22), 224106.
(53) Heyd, J.; Scuseria, G. E.; Ernzerhof, M. Hybrid functionals based on a screened Coulomb potential. *J. Chem. Phys.* **2003**, *118* (18), 8207−8215.
(54) Heyd, J.; Scuseria, G. E. Assessment and validation of a screened Coulomb hybrid density functional. *J. Chem. Phys.* **2004**, *120* (16), 7274−7280.
(55) Blöchl, P. E. Projector augmented-wave method. *Phys. Rev. B: Condens. Matter Mater. Phys.* **1994**, *50* (24), 17953−17979.
(56) Monkhorst, H. J.; Pack, J. D. Special points for Brillouin-zone integrations. *Phys. Rev. B: Solid State* **1976**, *13* (12), 5188−5192.
(57) Lide, D. R. CRC Handbook of Chemistry and Physics, 86th Edition Edited by David R. Lide (National Institute of Standards and Technology). CRC Press (an imprint of Taylor and Francis Group): Boca Raton, FL. 2005. 2544 pp. $125.96. ISBN 0-8493-0486-5. *J. Am. Chem. Soc.* **2006**, *128* (16), 5585.
(58) Burdett, J. K.; Hughbanks, T.; Miller, G. J.; Richardson, J. W., Jr.; Smith, J. V. Structural-electronic relationships in inorganic solids: powder neutron diffraction studies of the rutile and anatase polymorphs of titanium dioxide at 15 and 295 K. *J. Am. Chem. Soc.* **1987**, *109* (12), 3639−3646.
(59) Peters, G.; Vill, V. *Index of modern inorganic compounds. Subvolume A*; Landolt-Börnstein Numerical Data and Functional Relationships in Science and Technology: Verlag, Berlin, 1989.
(60) Vilela Oliveira, D.; Laun, J.; Peintinger, M. F.; Bredow, T. BSSE-correction scheme for consistent gaussian basis sets of double- and triple-zeta valence with polarization quality for solid-state calculations. *J. Comput. Chem.* **2019**, *40* (27), 2364−2376.
(61) Bruno, M.; Rubbo, M.; Pastero, L.; Massaro, F. R.; Nestola, F.; Aquilano, D. Computational Approach to the Study of Epitaxy: Natural Occurrence in Diamond/Forsterite and Aragonite/Zabuyelite. *Cryst. Growth Des.* **2015**, *15* (6), 2979−2987.
(62) Wang, V.; Xu, N.; Liu, J.-C.; Tang, G.; Geng, W.-T. VASPKIT: A user-friendly interface facilitating high-throughput computing and analysis using VASP code. *Comput. Phys. Commun.* **2021**, *267*, 108033.
(63) Momma, K.; Izumi, F. VESTA 3 for three-dimensional visualization of crystal, volumetric and morphology data. *J. Appl. Crystallogr.* **2011**, *44* (6), 1272−1276.
(64) Stukowski, A. Visualization and analysis of atomistic simulation data with OVITO-the Open Visualization Tool. *Modell. Simul. Mater. Sci. Eng.* **2010**, *18* (1), 015012.
(65) Hinuma, Y.; Grüneis, A.; Kresse, G.; Oba, F. Band alignment of semiconductors from density-functional theory and many-body perturbation theory. *Phys. Rev. B: Condens. Matter Mater. Phys.* **2014**, *90* (15), 155405.
(66) Harnett-Caulfield, L.; Walsh, A. Assessment of interstitial potentials for rapid prediction of absolute band energies in crystals. *J. Chem. Phys.* **2021**, *155* (2), 024113.
(67) Smidstrup, S.; Markussen, T.; Vancraeyveld, P.; Wellendorff, J.; Schneider, J.; Gunst, T.; Verstichel, B.; Stradi, D.; Khomyakov, P. A.; Vej-Hansen, U. G.; et al. QuantumATK: an integrated platform of electronic and atomic-scale modelling tools. *J. Phys.: Condens. Matter* **2020**, *32* (1), 015901.
(68) Trenczek-Zajac, A.; Banas-Gac, J.; Radecka, M. TiO2@Cu2O n-n Type Heterostructures for Photochemistry. *Materials* **2021**, *14* (13), 3725.
(69) Qi, L.; Wang, M.; Xue, J.; Zhang, Q.; Chen, F.; Liu, Q.; Li, W.; Li, X. Simultaneous Tuning Band Gaps of Cu2O and TiO2 to Form S-Scheme Hetero-Photocatalyst. *Chem.—Eur. J.* **2021**, *27* (59), 14638−14644.
(70) Cahen, D.; Kahn, A. Electron Energetics at Surfaces and Interfaces: Concepts and Experiments. *Adv. Mater.* **2003**, *15* (4), 271−277.
(71) Li, L.; Mi, J.; Yong, Y.; Mao, B.; Shi, W. First-principles study on the lattice plane and termination dependence of the electronic properties of the NiO/CH3NH3PbI3 interfaces. *J. Mater. Chem. C* **2018**, *6* (30), 8226−8233.
(72) Tasker, P. W. The stability of ionic crystal surfaces. *J. Phys. C: Solid State Phys.* **1979**, *12* (22), 4977−4984.

https://doi.org/10.1021/acsami.4c06081
ACS Appl. Mater. Interfaces 2024, 16, 35781−35792

(73) Noguera, C. Polar oxide surfaces. *J. Phys.: Condens. Matter* **2000**, *12* (31), R367−R410.
(74) Ohtake, A.; Mano, T.; Sakuma, Y. Strain relaxation in InAs heteroepitaxy on lattice-mismatched substrates. *Sci. Rep.* **2020**, *10* (1), 4606.
(75) Manasreh, O. *Semiconductor Heterojunctions and Nanostructures*; McGraw-Hill, Inc., 2005.
(76) Sze, S. M.; Ng, K. K. Physics and Properties of Semiconductors—A Review. In *Physics of Semiconductor Devices*; Wiley, 2006; pp 5−75.
(77) Di Liberto, G.; Pacchioni, G. Band offset in semiconductor heterojunctions. *J. Phys.: Condens. Matter* **2021**, *33* (41), 415002.
(78) Steiner, K.; Chen, W.; Pasquarello, A. Band offsets of lattice-matched semiconductor heterojunctions through hybrid functionals and ${G}_{0}{W}_{0}$. *Phys. Rev. B: Condens. Matter Mater. Phys.* **2014**, *89* (20), 205309.
(79) Baroni, S.; Resta, R.; Baldereschi, A.; Peressi, M. Can We Tune the Band Offset at Semiconductor Heterojunctions?. In *Spectroscopy of Semiconductor Microstructures*; Fasol, G., Fasolino, A., Lugli, P., Eds.; Springer US, 1989; pp 251−271.
(80) Van de Walle, C. G.; Martin, R. M. Theoretical study of band offsets at semiconductor interfaces. *Phys. Rev. B: Condens. Matter Mater. Phys.* **1987**, *35* (15), 8154−8165.
(81) Conesa, J. C. Modeling with Hybrid Density Functional Theory the Electronic Band Alignment at the Zinc Oxide-Anatase Interface. *J. Phys. Chem. C* **2012**, *116* (35), 18884−18890.
(82) Cerrato, E.; Gionco, C.; Paganini, M. C.; Giamello, E.; Albanese, E.; Pacchioni, G. Origin of Visible Light Photoactivity of the CeO2/ZnO Heterojunction. *ACS Appl. Energy Mater.* **2018**, *1* (8), 4247−4260.
(83) Shaltaf, R.; Rignanese, G. M.; Gonze, X.; Giustino, F.; Pasquarello, A. Band Offsets at the $\mathrm{Si}/{\mathrm{SiO}}_{2}$ Interface from Many-Body Perturbation Theory. *Phys. Rev. Lett.* **2008**, *100* (18), 186401.
(84) Mori-Sánchez, P.; Cohen, A. J.; Yang, W. Localization and Delocalization Errors in Density Functional Theory and Implications for Band-Gap Prediction. *Phys. Rev. Lett.* **2008**, *100* (14), 146401.
(85) Ramprasad, R.; Zhu, H.; Rinke, P.; Scheffler, M. New Perspective on Formation Energies and Energy Levels of Point Defects in Nonmetals. *Phys. Rev. Lett.* **2012**, *108* (6), 066404.
(86) Peressi, M.; Baldereschi, A.; Baroni, S. 2—Ab initio studies of structural and electronic properties. In *Characterization of Semiconductor Heterostructures and Nanostructures*; Lamberti, C., Ed.; Elsevier, 2008; pp 17−54.
(87) Alkauskas, A.; Broqvist, P.; Devynck, F.; Pasquarello, A. Band Offsets at Semiconductor-Oxide Interfaces from Hybrid Density-Functional Calculations. *Phys. Rev. Lett.* **2008**, *101* (10), 106802.
(88) Zhu, X.; Louie, S. G. Quasiparticle band structure of thirteen semiconductors and insulators. *Phys. Rev. B: Condens. Matter Mater. Phys.* **1991**, *43* (17), 14142−14156.
(89) Weston, L.; Tailor, H.; Krishnaswamy, K.; Bjaalie, L.; Van de Walle, C. G. Accurate and efficient band-offset calculations from density functional theory. *Comput. Mater. Sci.* **2018**, *151*, 174−180.
(90) Chen, W.; Pasquarello, A. Band-edge positions in GW: Effects of starting point and self-consistency. *Phys. Rev. B: Condens. Matter Mater. Phys.* **2014**, *90* (16), 165133.
(91) Aguirre, M. E.; Zhou, R.; Eugene, A. J.; Guzman, M. I.; Grela, M. A. Cu2O/TiO2 heterostructures for CO2 reduction through a direct Z-scheme: Protecting Cu2O from photocorrosion. *Appl. Catal., B* **2017**, *217*, 485−493.
(92) Liu, L.; Yang, W.; Sun, W.; Li, Q.; Shang, J. K. Creation of Cu2O@TiO2 Composite Photocatalysts with p-n Heterojunctions Formed on Exposed Cu2O Facets, Their Energy Band Alignment Study, and Their Enhanced Photocatalytic Activity under Illumination with Visible Light. *ACS Appl. Mater. Interfaces* **2015**, *7* (3), 1465−1476.
(93) Asadinamin, M.; Živkovic, A.; Ullrich, S.; Meyer, H.; Zhao, Y. Charge Dynamics of a CuO Thin Film on Picosecond to Microsecond Timescales Revealed by Transient Absorption Spectroscopy. *ACS Appl. Mater. Interfaces* **2023**, *15* (14), 18414−18426.
(94) Zhang, Y.-H.; Liu, M.-M.; Chen, J.-L.; Xie, K.-F.; Fang, S.-M. Dendritic branching Z-scheme Cu2O/TiO2 heterostructure photocatalysts for boosting H2 production. *J. Phys. Chem. Solids* **2021**, *152*, 109948.
(95) Messaadia, L.; Kiamouche, S.; Lahmar, H.; Masmoudi, R.; Boulahbel, H.; Trari, M.; Benamira, M. Solar photodegradation of Rhodamine B dye by Cu2O/TiO2 heterostructure: experimental and computational studies of degradation and toxicity. *J. Mol. Model.* **2023**, *29* (2), 38.

https://doi.org/10.1021/acsami.4c06081
ACS Appl. Mater. Interfaces 2024, 16, 35781−35792